ISSN 1392-1207. MECHANIKA. Vol. 32, No. 1, 2026: 39–48

Research on Error Characteristics Analysis and Error Compensation Methods for High-Precision Angular Measurement Turntables

Kun LI*, Weiquan WANG, Kunpeng WANG***, Xu YANG******

**Changchun Institute of Technology, Engineering Training Center, Changchun130012, Jilin, China, E-mail: likun@ccit.edu.cn (Corresponding Author)*

***Heilongjiang Academy of Agricultural Sciences, Soybean Institute, Harbin150086, Heilongjiang, China, E-mail: 2017200053@mails.cust.edu.cn*

****Changchun Institute of Meteorological Instruments Co., Ltd., Changchun130102, Jilin, China, E-mail: 1400033@ccit.edu.cn*

*****Jilin University, School of Mechanical and Aerospace Engineering, Changchun130012, Jilin, China, E-mail: yangxu@jlu.edu.cn*

https://doi.org/10.5755/j02.mech.42539

1. Introduction

High-precision angle measurement turntables serve as critical equipment in precision manufacturing, aerospace, defense industries, and other fields. With continuously escalating requirements for equipment manufacturing accuracy, more stringent performance demands are being placed on turntables. In recent years, significant breakthroughs have been achieved internationally in the field of high-precision angle measurement turntables [1-4]. The German PTB laboratory developed a dual-axis turntable system based on laser interferometers, which achieved a positioning accuracy of ±0.05″ by improving the installation error compensation algorithm [5]. The U.S. NIST employed a multi-readhead encoder system combined with Kalman filtering technology, effectively suppressing periodic errors of the turntable and achieving a dynamic measurement accuracy of 0.1″ [6]. The University of Tokyo developed an electromagnetic-driven turntable that reduced rotational errors to 0.03″ using active compensation technology [7]. Harbin Institute of Technology in China proposed a spherical harmonic function modeling method, enabling high-precision characterization of 17 error sources [8]. The National Institute of Metrology of China developed an air-bearing turntable system with a positioning accuracy of 0.02″ [9]. Tsinghua University in China created an online error compensation system, improving the turntable's repeat positioning accuracy by 40% [10].

Existing research primarily focuses on error separation, dynamic compensation, and leveling methods for high-precision angle measurement turntables to enhance their measurement accuracy and stability. This paper innovatively proposes an Opto-Mechanical coupled high-precision angle measurement turntable. Section 2 analyzes the structure and working mechanism of the high-precision angle measurement turntable. In Section 3, we establish the relative pose matrix model of the turntable system, develop the system error model, and conduct error characteristic analysis. Section 4 presents our research on error compensation methods for the turntable system. Section 5 verifies the feasibility and effectiveness of the error compensation for the high-precision angle measurement turntable system. Finally, conclusions are provided in Section 6.

2. Structural Analysis of High-Precision Angle Measurement Turntable

The high-precision angular measurement turntable mainly consists of a dual-axis turntable and optical components. The dual-axis turntable adopts a vertical dual-axis structure, with the inner and outer axes mutually coupled. Each axis is independently driven by torque motors I and II, respectively, and features position feedback from high-precision reference encoders I and II.

A tetrahedral prism at the lower end of the inner axis forms a small-angle measurement system with the autocollimator in the optical components. The upper end of the inner axis connects to the spindle of various components under test via a transition flange, enabling coaxial connection and synchronous transmission. The outer axis employs a split structure with upper and lower segments: the upper segment connects to the turntable table, while the lower segment supports the inner axis.

During angular measurement, based on the principle of reciprocal angular displacement measurement via counter-rotation [11], the inner and outer axes of the turntable rotate in opposite directions (forward and reverse). This enables continuous optical closed-loop angular metrology across the full 0 ~ 360° range for the component under test and the optical components. The structure of the high-precision angular measurement turntable is shown in Fig. 1.

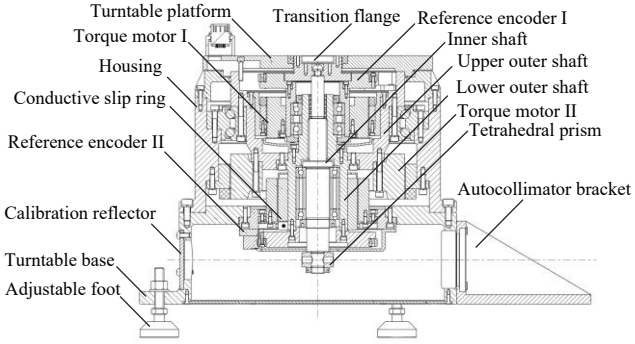

Fig. 1 Structure of high-precision measurement turntable

3. Error Principle Analysis

3.1. Establishment of system relative pose matrix

Based on the topological structure of the dual-axis turntable in the high-precision angular measurement system, coordinate systems are established including the system coordinate system $o_0x_0y_0z_0$, outer-axis coordinate system $o_1x_1y_1z_1$, inner-axis coordinate system $o_2x_2y_2z_2$, component-under-test shaft coordinate system $o_3x_3y_3z_3$, and optical component shaft coordinate system $o_4x_4y_4z_4$, where the system coordinate system $o_0x_0y_0z_0$ serves as the ideal reference frame while the optical component coordinate system $o_4x_4y_4z_4$functions as the actual reference frame.

Under ideal conditions, the system coordinate system coincides with both the inner and outer axis coordinate systems, while the optical component spindle and the component-under-test spindle remain collinear [12]. Assuming the outer axis rotation angle is α_i and the inner axis rotation angle is β_i, the schematic diagram of the dual-axis turntable system is shown in Fig. 2.

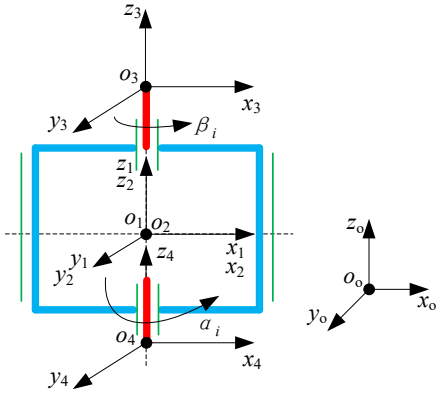

Fig. 2 Schematic diagram of the dual-axis turntable system

3.1.1. The pose transformation matrix of outer axis relative to system

Assume the coaxiality errors of the outer axis relative to the system are $\Delta\varepsilon_{x0}$ and $\Delta\varepsilon_{y0}$, the zero-position error is $\Delta\varphi_{z1}$, and the tilt rotation errors are $\Delta\sigma_{x1}(\alpha)$ and $\Delta\sigma_{y1}(\alpha)$. The rotation errors can be expressed by a second-order harmonic Fourier series expansion as follows:

$$\begin{cases} \Delta\sigma_{x1}(\alpha) = \Delta\sigma_{x1c}\cos 2\alpha + \Delta\sigma_{x1s}\sin 2\alpha \\ \Delta\sigma_{y1}(\alpha) = \Delta\sigma_{y1c}\cos 2\alpha + \Delta\sigma_{y1s}\sin 2\alpha \end{cases}, \tag{1}$$

where: $\Delta\sigma_{x1c}$, $\Delta\sigma_{x1s}$, $\Delta\sigma_{y1c}$ and $\Delta\sigma_{y1s}$ represent the amplitudes of the cosine and sine terms in the second-order harmonic components of the outer axis's tilt rotation errors. Therefore, the pose transformation matrix of the outer axis relative to the system is given by:

$$C_1^0 = R(x_0,\Delta\varepsilon_{x0})R(y_0,\Delta\varepsilon_{y0})R(x_0,\Delta\sigma_{x1}(\alpha)), \\ R(y_0,\Delta\sigma_{y1}(\alpha))R(z_0,\alpha)R(z_1,\Delta\varphi_{z1}). \tag{2}$$

where: $R(v, \theta)$ represents the unit pose transformation matrix formed $\boldsymbol{v} = x_j, y_j, z_j$ by rotating angle θ about axis v, and $j = 0, 1, 2, 3, 4$; φ denotes the angular error of each axis rotation. Therefore, the unit transformation matrices about the x-axis, y-axis, and z-axis are respectively:

$$R(x,\theta) = \begin{bmatrix} 1 & 0 & 0 \\ 0 & C\theta & -S\theta \\ 0 & S\theta & C\theta \end{bmatrix}, \quad R(y,\theta) = \begin{bmatrix} C\theta & 0 & S\theta \\ 0 & 1 & 0 \\ -S\theta & 0 & C\theta \end{bmatrix}, \\ R(z,\theta) = \begin{bmatrix} C\theta & -S\theta & 0 \\ S\theta & C\theta & 0 \\ 0 & 0 & 1 \end{bmatrix}.$$

3.1.2. The pose transformation matrix of inner axis relative to outer axis

Assume the coaxiality errors of inner axis relative to outer axis is $\Delta\varepsilon_{x1}$ and $\Delta\varepsilon_{y1}$, the zero-position error is $\Delta\varphi_{z2}$, and the tilt rotation errors are $\Delta\sigma_{x2}(\beta)$ and $\Delta\sigma_{y2}(\beta)$. The rotation errors can be expressed by the second-order harmonic Fourier series expansion as follows:

$$\begin{cases} \Delta\sigma_{x2}(\beta) = \Delta\sigma_{x2c}cos2\beta + \Delta\sigma_{x2s}sin2\beta \\ \Delta\sigma_{y2}(\beta) = \Delta\sigma_{y2c}cos2\beta + \Delta\sigma_{y2s}sin2\beta \end{cases}, \tag{3}$$

where: $\Delta\sigma_{x2c}$, $\Delta\sigma_{x2s}$, $\Delta\sigma_{y2c}$ and $\Delta\sigma_{y2s}$ represent the amplitudes of the cosine and sine terms in the second-order harmonics of the inner axis's tilt rotation errors. Thus, the pose transformation matrix of the inner axis relative to the outer axis is given by:

$$C_2^1 = R(x_1,\Delta\varepsilon_{x1})R(y_1,\Delta\varepsilon_{y1})R(x_1,\Delta\sigma_{x2}(\beta)), \\ R(y_1,\Delta\sigma_{y2}(\beta))R(z_1,\beta)R(z_2,\Delta\varphi_{z2}). \tag{4}$$

3.1.3. The pose transformation matrix of optical assembly relative to inner axis

Assume the installation errors between the inner axis and optical assembly are $\Delta\tau_{x0}$ and $\Delta\tau_{y0}$, the pose transformation matrix of the optical assembly relative to the inner axis is given by:

$$C_4^2 = C_0^2 = R(x_0,\Delta\tau_{x0})R(y_0,\Delta\tau_{y0})R(z_0,\alpha). \tag{5}$$

3.1.4. The pose transformation matrix of test component relative to reference system

Assume the initial zero-position error of test component spindle is $\Delta\tau_{z3}$, the mounting errors relative to turntable platform are $\Delta\tau_{x3}$ and $\Delta\tau_{y3}$. The pose transformation matrix of the test component spindle relative to the reference system is expressed as:

$$C_3^0 = R(x_3,\Delta\tau_{x3})R(y_3,\Delta\tau_{y3})R(z_3,\Delta\tau_{z3}). \tag{6}$$

3.2. Establishment of system error model

Considering the random variations in the input parameters of the component under test, this paper employs a vertical dual-axis turntable structure with inner and outer axes. The rotary positioning accuracy after simultaneous and co-directional constant-speed rotation (speed < 25 (°/s))

of the turntable is taken as the target value for error analysis. This operating condition encompasses the most complex error coupling state of the system under quasi-static loading. And the spatial coupling pose matrix of the system's output angular position is expressed as:

$$\begin{bmatrix} \Delta s_x \\ \Delta s_y \\ \Delta s_O \end{bmatrix} = \left(C_2^1 C_4^2 C_3^0\right)^T \begin{bmatrix} 1 \\ 1 \\ \lambda \end{bmatrix} = \left(C_2^1 C_0^2 C_3^0\right)^T \begin{bmatrix} 1 \\ 1 \\ \lambda \end{bmatrix} = \\ = \left(C_2^1 C_0^2 C_3^0\right)^T \begin{bmatrix} 1 & 1 & \lambda \end{bmatrix}^T. \quad (7)$$

where: $[1\ 1\ \lambda]^T$ represents the error component generated by the angular position matrix of the component under test on the main shaft. Δs_x, Δs_y and Δs_o respectively denote the error components of the angular position of the component under test's main shaft relative to the x-axis, y-axis, and system O-axis.

By substituting the relative pose matrices of each axis and the unit pose matrix $R(\nu, \theta)$ into the spatial coupling pose matrix respectively, the error components of the main shaft angular position of the component under test relative to the x-axis, y-axis are obtained as follows:

$$\begin{cases} \Delta s_x = \left(\Delta\varepsilon_{x1} + \Delta\sigma_{x2}(\beta)\right)\Delta\tau_{x0}\Delta\tau_{x3}\cos\beta - \\ \quad -\left(\Delta\varepsilon_{x1} + \Delta\sigma_{x2}(\beta)\right)\Delta\tau_{y0}\Delta\tau_{y3}\cos\alpha\sin\beta - \\ \quad -\lambda\left(\Delta\varepsilon_{x1} + \Delta\sigma_{x2}(\beta)\right)\Delta\tau_{y0}\Delta\tau_{z3}\sin\alpha\sin\beta, \\ \Delta s_y = \left(\Delta\varepsilon_{y1} + \Delta\sigma_{y2}(\beta)\right)\Delta\tau_{x0}\Delta\tau_{x3}\sin\beta + \\ \quad +\left(\Delta\varepsilon_{y1} + \Delta\sigma_{y2}(\beta)\right)\Delta\tau_{y0}\Delta\tau_{y3}\cos\alpha\cos\beta + \\ \quad +\lambda\left(\Delta\varepsilon_{y1} + \Delta\sigma_{y2}(\beta)\right)\Delta\tau_{y0}\Delta\tau_{z3}\sin\alpha\cos\beta. \end{cases} \quad (8)$$

The error component of the system O-axis is:

$$\Delta s_O = \Delta\varphi_{z2}\Delta\tau_{y3}\sin\alpha + \lambda\Delta\varphi_{z2}\Delta\tau_{y3}\cos\alpha. \quad (9)$$

Considering the coupling of spatial geometric errors, the system error model is expressed as:

$$\Delta e = D_O\Delta s_O + D_x\Delta s_x + D_y\Delta s_y + \\ + D_{xy}\Delta s_x\Delta s_y + D_{xx}\Delta s_x{}^2 + D_{yy}\Delta s_y{}^2 + \Delta\delta. \quad (10)$$

where: D_O represents the sensitivity coefficient of the system's main shaft, D_x, D_y, and D_{xy} denote the sensitivity coefficients of the system's main shaft relative to the x-axis, y-axis and the cross-coupling term between the x-axis and y-axis, respectively. D_{xx} and D_{yy} are the quadratic nonlinear coefficients for the x and y axes, respectively, and $\Delta\delta$ represents the system residual error.

Neglecting the influence of higher-order small quantities and assuming the second-order accuracy coefficient approximates the error component as $\Delta s_x'$ and $\Delta s_y'$, with the second-order accuracy adjustment coefficient being γ, the approximate values of the error components are given as:

$$\begin{cases} \Delta s_x' = \gamma_x\left(\Delta\varepsilon_{x1} + \Delta\sigma_{x2}(\beta)\right)\Delta\tau_{x0}\Delta\tau_{x3}\cos\beta \\ \Delta s_y' = \gamma_y\left(\Delta\varepsilon_{y1} + \Delta\sigma_{y2}(\beta)\right)\Delta\tau_{y0}\Delta\tau_{y3}\cos\alpha\cos\beta \end{cases}. \quad (11)$$

3.3. Analysis of system error characteristics

The accuracy coefficients of the turntable system's main spindle and the test component's spindle relative to the x-axis and y-axis influence the precision of the calibrated system's output angle. Structural errors in the dual-axis turntable introduce systematic errors into the output values of the test component.

Among these, the accuracy coefficients D_O, D_x, D_y, D_{xy}, D_{xx} and D_{yy} of the system's axis represent fixed error sources, while the coaxiality errors $\Delta\varepsilon$, the tilt rotation errors $\Delta\sigma$, the zero-position errors $\Delta\varphi$, and component installation errors $\Delta\tau$ of the inner/outer spindles and test component's spindle constitute variable error sources.

The method integrates the full-combination constant-angle approach with dual-axis reciprocal rotation by employing a set of appropriate and relatively stable reference rotation angles β for independent comparison with the test component's output angles, thereby eliminating the influence of zero-position errors $\Delta\varphi$ in the system's inner/outer axes and the test component's spindle as well as component installation errors $\Delta\tau$ ($\Delta\varphi \to 0$, $\Delta\tau \to 0$) to establish error-free reference angles β.

Based on the comprehensive error model of the test component on the dual-axis turntable, the angle compensation system utilizes angular position feedback from the inner/outer axis reference encoders and baseline angle acquisition from the autocollimator to achieve full-range compensation of coaxiality errors $\Delta\varepsilon$ and tilt rotation errors $\Delta\sigma$ ($\lambda = 1$, $\gamma \to 0$) between both axes.

Through the feed-forward mechanism of the system error model, the system processes real-time data from reference encoders I/II and the autocollimator detection unit to acquire current dual-axis angles and system variable errors (including coaxiality and tilt rotation errors), which are then computationally combined with target angles and fed into the drive control system to accomplish full-circumference angular error compensation.

Combining the error elimination of the reference angle with the full-range error compensation algorithm, and integrating Eq. (7) to Eq. (11), the original system spatial error model is established.

Under the premise of ensuring computational accuracy, the original model is simplified by neglecting higher-order small quantities and focusing on the second harmonic components of the rotary error, ultimately yielding the approximate system spatial error model as follows:

$$\Delta e_{ca} = D_O\cos\alpha + D_x\left(\Delta\varepsilon_{x1} + \Delta\sigma_{x2c}\cos 2\beta + \Delta\sigma_{x2s}\sin 2\beta\right)\cos\beta + \\ + D_y\left(\Delta\varepsilon_{y1} + \Delta\sigma_{y2c}\cos 2\beta + \Delta\sigma_{y2s}\sin 2\beta\right)\cos\alpha\cos\beta + \\ + D_{xy}\left[\left(\Delta\varepsilon_{x1} + \Delta\sigma_{x2c}\cos 2\beta + \Delta\sigma_{x2s}\sin 2\beta\right)\cos\beta\right]\left[\left(\Delta\varepsilon_{y1} + \Delta\sigma_{y2c}\cos 2\beta + \Delta\sigma_{y2s}\sin 2\beta\right)\cos\alpha\cos\beta\right]. \quad (12)$$

The sensitivity coefficient D_O of the system's main spindle and the sensitivity coefficients D_x, D_y, and D_{xy} of the test component's spindle relative to the x-axis, y-axis and their cross-coupling terms are fixed error factors with relatively minor influence, which are neglected here. It can be derived from the system spatial error model in Eq. (12) that the coaxiality errors $\Delta\varepsilon_{x1}$ and $\Delta\varepsilon_{y1}$, of the inner shaft axis relative to the outer shaft axis, along with the second-order harmonic terms $\Delta\sigma_{x2c}$, $\Delta\sigma_{x2s}$, $\Delta\sigma_{y2c}$ and $\Delta\sigma_{y2s}$ of the inner axis's tilt rotation errors, constitute the primary influencing factors of system errors.

The coaxiality and tilt rotation errors of the dual-axis turntable's inner axis significantly affect the system's spatial angular positioning accuracy, thereby introducing systematic errors into the calibrated output values. Consequently, this study employs rational matching and error compensation methods to control these four dominant geometric errors within permissible limits, thereby ensuring system precision.

The establishment of this approximate system spatial error model is based on clearly defined operating boundaries. Regarding environmental conditions, the model assumes a standard laboratory temperature (20°C ± 1°C). Under this baseline, all coaxiality errors $\Delta\varepsilon_{x1}$ and $\Delta\varepsilon_{y1}$, tilt error coefficients $\Delta\sigma_{x2c}$, $\Delta\sigma_{x2s}$, $\Delta\sigma_{y2c}$ and $\Delta\sigma_{y2s}$ are treated as fixed parameters. Regarding loading conditions, the validity of the model is confined to light-load or quasi-static loading scenarios, where load-induced deformation errors are negligible and thus disregarded. Regarding motion conditions, the model takes constant-speed rotation as its research object. It primarily compensates for the geometric error components related to angular position and the second harmonic terms of the rotary error, ensuring high compensation stability under low-to-medium constant-speed conditions.

4. System Error Compensation

The system error compensation is achieved through comprehensive analysis of the complete error model of the test component on the measurement turntable and system error characteristics: the influence of fixed system errors is eliminated by averaging multiple measurements and implementing artificial neural network algorithm compensation; full-range reference rotation angle error cancellation is accomplished using the full-circle closure principle and reciprocal sequential comparison method with external metrological standards; the three-point reverse error separation algorithm is employed to compensate for variable errors such as installation misalignment between the test component and measurement turntable. By establishing a mapping function between the dual-axis turntable and test component, continuous mutual compensation of turntable system errors and test component rotation errors across the full range is realized, mitigating the impact of other variable errors on the calibration system and ensuring the calibration accuracy of the optical continuous closed-loop calibration system.

4.1. Compensation algorithm for installation eccentricity errors of test components

During precision calibration, the installation errors of test components constitute the most significant factor among all component mounting errors. In practical calibration processes, the main spindle of the test component is integrated with the inner axis fixture of the dual-axis turntable through a specialized flange. Due to installation and machining tolerances, perfect coaxial alignment between the test component's spindle centerline and the turntable's inner axis centerline cannot be achieved, inevitably introducing installation eccentricity errors during the fixturing process.

To ensure calibration accuracy of test components, a compensation algorithm based on the three-point reverse error separation method is employed to mitigate these eccentricity errors. The detection principle of eccentricity errors using the three-point method is illustrated in Fig. 3.

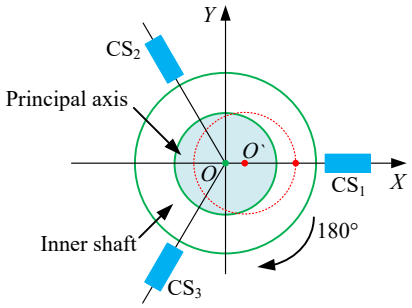

Fig. 3 Principle of eccentricity error measurement

4.1.1. Eccentricity error modeling of spindle based on three-point method

The three-point method employs three capacitance sensors, CS_1, CS_2 and CS_3, uniformly spaced around the circumference at installation angles of 0°, 120°, and 240°, respectively. The projection relationship of each sensor within the X-Y plane can be described as follows: CS_1 is oriented along the positive X-axis, CS_2 is oriented at 120° relative to the X-axis, and CS_3 is oriented at 240° relative to the X-axis. Consequently, a unified Cartesian coordinate system can be established to synthesize the error components.

From the data acquired by capacitance sensors CS_1, CS_2 and CS_3, the roundness error $D(\varphi)$ of the spindle of the component under test, as well as its eccentricity error component $X(\varphi)$ along the X-axis, are calculated. The eccentricity error component $Y(\varphi)$ along the Y-axis is determined using the data collected by CS_2 and CS_3. The overall eccentricity error $E(\varphi)$ of the spindle is then obtained by synthesizing the eccentricity error components along the X-axis and Y-axis.

At the error sampling point at position "φ_0", the error signals acquired by the three capacitance sensors are:

$$CS_1(\varphi_0) = D(\varphi_0) + X(\varphi_0)\,, \tag{13}$$

$$CS_2(\varphi_0) = D\left(\varphi_0 + \frac{2\pi}{3}\right) + X(\varphi_0)\cos\frac{2\pi}{3} + Y(\varphi_0)\sin\frac{2\pi}{3} = D\left(\varphi_0 + \frac{2\pi}{3}\right) - \frac{1}{2}X(\varphi_0) + \frac{\sqrt{3}}{2}Y(\varphi_0)\,, \tag{14}$$

$$CS_3(\varphi_0) = D\left(\varphi_0 + \frac{4\pi}{3}\right) + X(\varphi_0)\cos\frac{4\pi}{3} + Y(\varphi_0)\sin\frac{4\pi}{3} = D\left(\varphi_0 + \frac{4\pi}{3}\right) - \frac{1}{2}X(\varphi_0) - \frac{\sqrt{3}}{2}Y(\varphi_0)\,. \tag{15}$$

The radial rotation error of the test component's spindle is uncontrollable but exhibits periodic variations, which can be solved using Fourier transform. Since Fourier transform primarily consists of low-order (first four) harmonic components with negligible influence from higher-order harmonics, and given that the spindle's radial rotation error is predominantly composed of odd harmonics, an inverse separation algorithm is employed to isolate the even harmonics and determine the spindle's radial rotation error [13].

When only even harmonics exist in the Fourier transform, the eccentricity error component along the X-axis at the error sampling point at position "φ_0" is:

$$X(\varphi_0)=X(\varphi_0+\pi). \tag{16}$$

Similarly, the eccentricity error component along the Y-axis of the spindle at the error sampling point at position "φ_0" is:

$$Y(\varphi_0)=CS_2(\varphi_0)+CS_3(\varphi_0)-D\left(\varphi_0+\frac{\pi}{2}\right). \tag{17}$$

By orthogonally combining the two sets of error data from eccentricity error components $X(\varphi_i)$ and $Y(\varphi_i)$, the total eccentricity error $E(\varphi_i)$ of the test component's spindle in the two-dimensional plane is derived as:

$$E(\varphi_i)=\sqrt{X(\varphi_i)^2+Y(\varphi_i)^2}. \tag{18}$$

The installation eccentricity error of the spindle corresponds to the first harmonic component in the Fourier transform of the spindle's radial rotational error, and since the first harmonic represents the dominant constituent of the installation eccentricity error signal, the spindle's installation eccentricity error can be determined by isolating the first harmonic from the Fourier transform.

Through data acquisition using three capacitive sensors CS_1, CS_2, and CS_3 followed by Fourier transform processing, the first harmonic Fourier coefficients for CS_1, CS_2, and CS_3 are respectively given as:

$$\begin{cases} a_{11}=\dfrac{2}{n}\left[\sum_{i=0}^{n-1}CS_1(\varphi_i)\cdot cos(\varphi_i)\right] \\ b_{11}=\dfrac{2}{n}\left[\sum_{i=0}^{n-1}CS_1(\varphi_i)\cdot sin(\varphi_i)\right] \end{cases}, \tag{19}$$

$$\begin{cases} a_{12}=\dfrac{2}{n}\left[\sum_{i=0}^{n-1}CS_2(\varphi_i)\cdot cos(\varphi_i)\right] \\ b_{12}=\dfrac{2}{n}\left[\sum_{i=0}^{n-1}CS_2(\varphi_i)\cdot sin(\varphi_i)\right] \end{cases}, \tag{20}$$

$$\begin{cases} a_{13}=\dfrac{2}{n}\left[\sum_{i=0}^{n-1}CS_3(\varphi_i)\cdot cos(\varphi_i)\right] \\ b_{13}=\dfrac{2}{n}\left[\sum_{i=0}^{n-1}CS_3(\varphi_i)\cdot sin(\varphi_i)\right] \end{cases}. \tag{21}$$

When spindle installation eccentricity exists, the data relationships for capacitive sensors CS_1, CS_2, and CS_3 are characterized as follows:

$$\begin{cases} CS_1'(\varphi_i)=a_{11}\cdot cos(\varphi_i)+b_{11}\cdot sin(\varphi_i) \\ CS_2'(\varphi_i)=a_{12}\cdot cos(\varphi_i)+b_{12}\cdot sin(\varphi_i) \\ CS_3'(\varphi_i)=a_{13}\cdot cos(\varphi_i)+b_{13}\cdot sin(\varphi_i) \end{cases}. \tag{22}$$

The roundness error $D'(\varphi_i)$ of the spindle after separation of the first harmonic is:

$$D'(\varphi_i)=CS_1'(\varphi_i)+CS_2'\left(\varphi_i+\frac{2\pi}{3}\right)+CS_3'\left(\varphi_i+\frac{4\pi}{3}\right). \tag{23}$$

The eccentricity error components along the X-axis and Y-axis, denoted as $X'(\varphi_i)$ and $Y'(\varphi_i)$ respectively, are:

$$X'(\varphi_i)=CS_1'(\varphi_i)-D'(\varphi_i), \tag{24}$$

$$Y'(\varphi_i)=\frac{CS_2'(\varphi_i)-D'\left(\varphi_i+\frac{2\pi}{3}\right)-X'(\varphi_i)cos\frac{2\pi}{3}}{sin\frac{2\pi}{3}}=\frac{CS_2'(\varphi_i)-D'\left(\varphi_i+\frac{2\pi}{3}\right)+\frac{1}{2}X'(\varphi_i)}{\frac{\sqrt{3}}{2}}. \tag{25}$$

The spindle eccentricity error $E'(\varphi_i)$ is obtained through orthogonal synthesis of two sets of error data (eccentricity error components $X'(\varphi_i)$ and $Y'(\varphi_i)$ after three-point method reverse error separation, expressed as:

$$E'(\varphi_i)=\sqrt{X'(\varphi_i)^2+Y'(\varphi_i)^2}. \tag{26}$$

Next, the raw data collected using the three-point reverse error separation algorithm represents coupled signals comprising spindle installation eccentricity errors, spindle/flange roundness errors, and noise errors. The interference data is filtered and noise errors are eliminated through digital signal processing and test-point averaging methods. The pre-processed error components are then used to synthesize spindle installation eccentricity error data, which is subsequently employed for system error compensation.

4.1.2. Simulation analysis of three-point reverse eccentricity error separation algorithm

To validate the effectiveness of the three-point reverse eccentricity error separation algorithm, MATLAB was employed to conduct simulation analysis using normally distributed eccentricity error data with randomized parameters, where the simulation system utilized 360 sampling points with spindle eccentricity data generated as normally distributed random numbers, incorporating three circumferentially arranged capacitive sensors CS_1, CS_2 and CS_3 at installation angles of 0°, 120°, and 240° respectively,

and the circular plot comparing pre-simulation and post-simulation error data superposition results on a 30nm radius base circle is shown in Fig. 4.

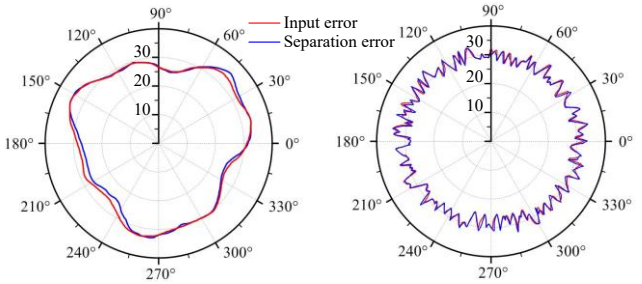

a b

Fig. 4 Comparison of circular plots: a – roundness error, b – eccentricity error

Through the comparative analysis of the maximum amplitude differences before and after error separation in the circular image of Fig. 4: the maximum amplitude difference of the separated spindle roundness error is approximately 3.98% smaller than its error amplitude, and the maximum amplitude difference of the spindle eccentricity error is approximately 2.93% smaller than its error amplitude. This indicates that the three-point method reverse error separation algorithm achieves a favorable error separation effect for random spindle eccentricity errors.

When the spindle installation has an eccentricity of $e = 1$ μm, the calculation results of Eq. (12) can be represented in polar coordinates. The error data plots before and after eccentricity compensation is shown in Fig. 5.

As can be seen from Fig. 5, the center of the compensated error plot essentially coincides with the origin of the polar coordinates, demonstrating that the three-point reverse error separation algorithm can effectively compensate for spindle eccentricity errors. This improvement enhances the radial rotation accuracy of the spindle and ensures the calibration precision of the system.

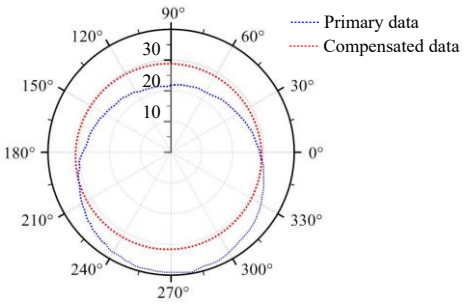

Fig. 5 Comparative diagram of circular plots before and after eccentricity error compensation

4.2. Particle swarm optimization for error compensation in BP neural networks

The modified particle swarm optimization (MPSO) algorithm was applied to optimize the BP neural network model for systematic error compensation in a dual-axis turntable system, establishing an MPSO-optimized BP neural network model [14-15]. The specific algorithm workflow (Fig. 6) is as follows:

Step 1: Initialize the BP neural network structure, and determine the influencing factors of system errors, including the inner axis angle, outer axis angle, auto-collimation angle, and the angle error of the component under test, which serve as the inputs to the BP neural network.

Step 2: Use the MPSO algorithm to initialize parameters, determining the initial inertia factor and the initial values of the learning factors.

Step 3: Optimize the initial BP neural network using the MPSO algorithm, and iteratively update the initial weights and thresholds.

Step 4: Further divide the pre-processed training sample set into a training subset and a validation subset. Use the training subset for the MPSO-BP neural network to learn error characteristics, while using the validation subset to monitor the generalization ability of the model. During the training process, monitor training to prevent over-fitting, thereby determining the optimal MPSO-BP neural network model for the compound dual-axis turntable.

Step 5: Adjust the initial weights of the BP neural network, determine the thresholds, and analyze whether the algorithm falls into a local optimum. If it falls into a local optimum, continue iterating and return to Step 3， otherwise, end the iteration and proceed to Step 6.

Step 6: Determine the optimal weights and thresholds of the MPSO-BP neural network model.

Step 7: Complete the establishment of the error compensation model for the compound dual-axis turntable based on the MPSO-BP neural network, and output the processed data.

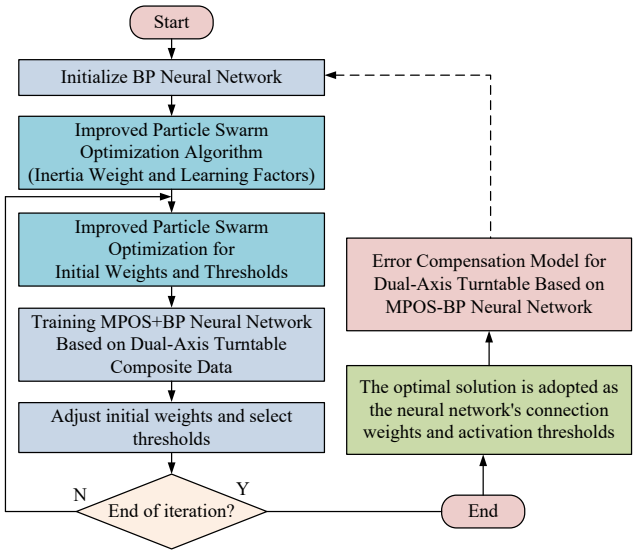

Fig. 6 Flowchart of the MPSO-BPNN Model

4.3. Simulation analysis of the system error compensation

The experiment takes the measured data collected by the compound dual-axis calibration system as the research object. Within the full range of 0° to 360°, 360 sets of sample data (standard values and measured values) are recorded, and the pre-processed sample data are normalized. To fully verify the generalization ability of the model and prevent over-fitting, the dataset is divided as follows:

Training set and test set: 320 sets of sample data are randomly selected as the training set (for model parameter learning), and the remaining 40 sets are used as the test set (for unbiased evaluation of the final model performance).

Validation set: During the model training process, to monitor the training status and guide hyper-parameter

adjustment, 270 sets are further randomly divided from the 320-set training set as the training subset, and 50 sets are used as the validation subset. The validation set does not participate in weight updates and is only used to evaluate the generalization error of the model after each iteration.

Based on this dataset, a 2×35×2 BP neural network model is established, employing {'tansig','purelin'} as transfer functions and the gradient descent method as the training algorithm. For the MPSO algorithm configuration, the population size was set to 40 with a maximum iteration count of 200, a preset error threshold of 10^{-1}. The initial inertia factor ω_{max} and final inertia factor ω_{min} were set to 0.9 and 0.3 respectively, while the initial learning factor $c_{1,2max}$ and final learning factor $c_{1,2min}$ were assigned values of 1 and 3 respectively, with each dimensional position and velocity of the initialized particles being random numbers within the range [0, 1].

The MPSO+BP neural network model underwent iterative training to continuously update initial weights and thresholds while learning system error characteristics. After 110 iterations (Fig. 7) meeting the required criteria, the improved particle swarm optimization algorithm decoded and assigned the optimized initial weights and thresholds to the BP neural network. By utilizing the trained global best positions, the model determined optimal weights and thresholds for the MPSO+BP neural network, ultimately establishing a composite dual-axis turntable MPSO+BP neural network model.

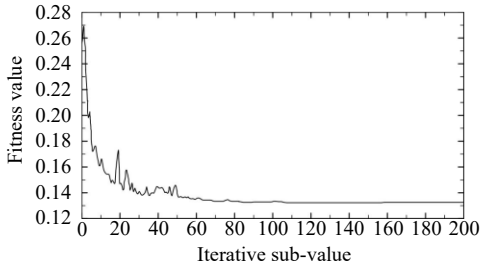

Fig. 7 Fitness curve of the MPSO

MATLAB simulations were conducted to compare the system error compensation performance between the BP neural network and MPSO+BP neural network models, with uncompensated data serving as the baseline. The error comparisons before and after compensation are presented in Fig. 8 and Table 1. Analysis of the comparison curves reveals: uncompensated system errors ranged between 3″ to 4″, while traditional BP neural network compensation reduced output errors to within ±1″. Notably, the MPSO+BP neural network compensation achieved superior performance with overall output errors below ±0.5″, demonstrating significant calibration accuracy improvement and more stable error distribution.

Experimental data comparisons demonstrate that after MPSO+BP neural network error compensation, the mean absolute error (MAE), root mean square error (RMSE), and system testing error were significantly reduced. Specifically, the MAE decreased to 0.102 and RMSE to 0.119. Compared with uncompensated results, system accuracy improved from 0.138% to 0.012%, representing a 91.30% overall enhancement. Furthermore, relative to BP neural network compensation alone, the system accuracy increased from 0.046% to 0.012%, achieving a 73.91% overall

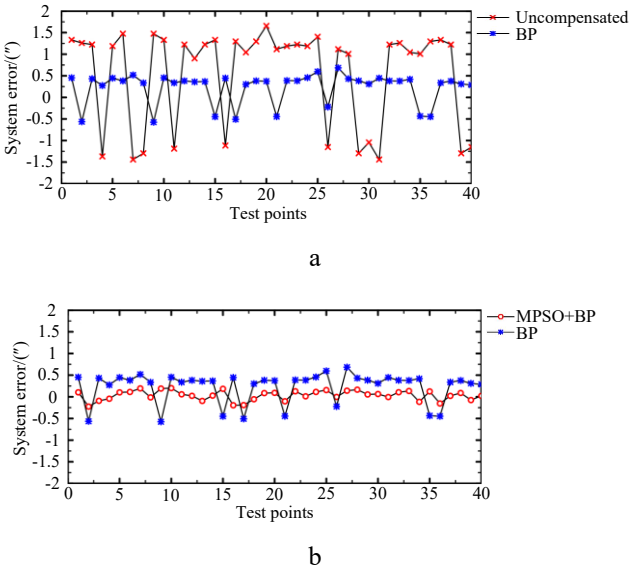

Fig. 8 Error comparison before and after MPSO-BP compensation: a – BP network, b – MPSO+BP network

Table 1
Error comparison before and after compensation

Algorithm	MAE/(″)	RMSE/(″)	Precision/(%FS)
Uncompensated	1.240	1.251	0.138
BP	0.412	0.422	0.046
MPSO+BP	0.102	0.119	0.012

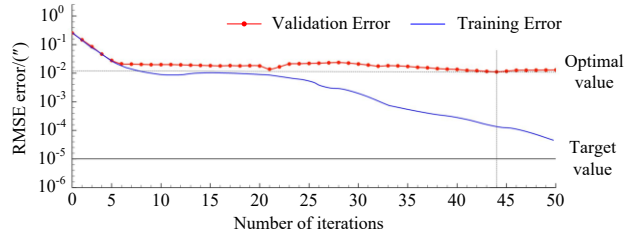

Fig. 9 Error monitoring curves during the training process of the MPSO-BP neural network

improvement, thereby validating the superior compensation effectiveness of the MPSO+BP model.

To verify the generalization ability of the MPSO-BP neural network model and avoid over-fitting, Fig. 9 presents the error variation curves of the training set and validation set during the training process.

It can be observed from the figure that as the number of iterations increases, both the training set error and the validation set error exhibit a synchronous downward trend and stabilize after 44 iterations. When approaching the optimal solution, the validation set error does not show any significant rebound or increase, indicating that the model has not experienced over-fitting during the training process and possesses good generalization ability.

To validate the learning efficiency of the MPSO+BP neural network-based dual-axis system error compensation model, comparative learning tests were conducted under identical sample data conditions using both BP and MPSO+BP neural networks. The contrasting iteration curves of system error training are presented in Fig. 10.

Analysis of the error training curves in Fig. 10 reveals: when reducing errors to 0.1″, the BP neural network

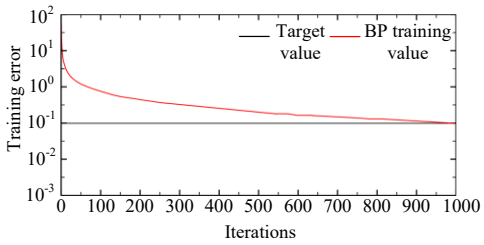

a

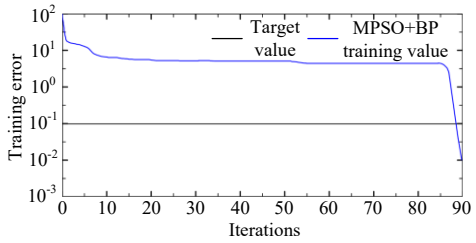

b

Fig. 10 Iterative training curves of system error compensation using MPSO+BP: a – BP neural network, b – MPSO+BP neural network

model required approximately 1000 iterations, whereas the MPSO+BP neural network model achieved the same error threshold in merely 88 iterations. This demonstrates that the MPSO+BP dual-axis system error compensation model exhibits significantly higher learning efficiency compared to the conventional BP neural network approach. By introducing the validation set monitoring mechanism, the reliability and robustness of the MPSO-BP neural network in compensating for the system errors of the compound dual-axis turntable are effectively ensured.

5. Precision Measurement Experiment

5.1. System calibration experiment

The system calibration experiment implemented strict control over key influencing factors, conducted in a laboratory with stable temperature (20 °C) and humidity (50% RH) conditions along with effective vibration isolation. Precision calibration was performed using a high-accuracy optical autocollimator (measurement range: 0′ ~ 10′, resolution: 0.01″, accuracy: 0.2″, Grade 2) and a 23-faced optical polygon (measurement range: 0°~360°, Grade 3).

The experimental setup for precision calibration is shown in Fig. 11. And the system accuracy was calibrated using the full-combination method and full-circle closure principle, with the resulting accuracy calibration curve shown in Fig. 12.

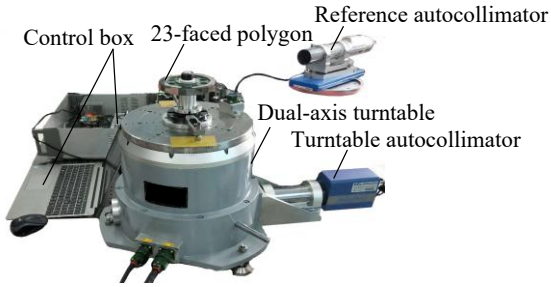

Fig. 11 System accuracy calibration test bench

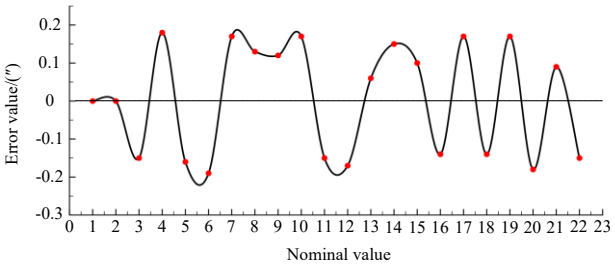

Fig. 12 System accuracy calibration curve

The system accuracy calibration curve demonstrates: a zero-start error of 0.00″, maximum error of ±0.19″, and post-calibration system accuracy of 0.38″ (peak-to-peak), meeting the requirements for high-precision (sub-arcsecond accuracy) and full-circle continuous calibration.

5.2. System application verification

The precision comparative verification was conducted in a laboratory with controlled temperature (19.9°C) and humidity (52% RH) conditions and effective vibration isolation, using the calibrated system to evaluate a JZN-1 high-precision photoelectric angle encoder (factory specifications: resolution 0.01″, accuracy ±0.5″) manufactured by an industrial enterprise. Among them, the precision comparison curves of the experimental platform and the system before and after compensation are shown in Fig. 13 and Fig. 14 respectively.

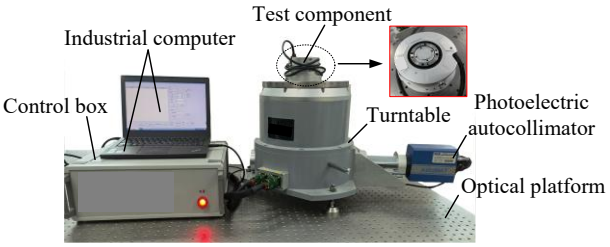

Fig. 13 Comparative test bench for calibration system

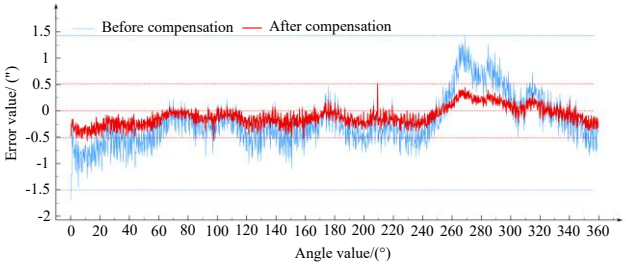

Fig. 14 Comparative accuracy curve

Analysis of the accuracy comparison curve in Fig. 14 reveals that the system's calibrated accuracy after error compensation is fundamentally consistent with the factory-calibrated accuracy of the JZN-1 encoder. However, due to measurement environmental interference and instrument fluctuations at different sampling points, certain sampling points exhibit relatively large measurement errors or fluctuations. Nevertheless, the overall post-compensation error distribution remains within ±0.5″ (compared to ±1.5″ before compensation), thereby verifying that the system meets the practical requirements for high-precision, full-range continuous calibration.

6. Conclusions

To address the insufficient accuracy of traditional angle measurement turntable calibration techniques, this study proposes a high-precision angle measurement turntable based on Opto-Mechanical coupling principles and reciprocal angular displacement measurement methods. Using multi-body system theory and relative pose matrix transformation methods, a comprehensive error model for the dual-axis turntable was established. The three-point reverse error separation algorithm and dual-axis continuous error compensation algorithm were employed to effectively compensate for installation errors. Furthermore, an improved particle swarm optimization (MPSO) algorithm was utilized to optimize the BP neural network model for system error compensation. Simulation analyses verified the effectiveness of the MPSO-BP neural network model in compensating system errors. Calibration and application experiments conducted with the compensated system yielded the following conclusions:

1. An error model for high-precision angle measurement turntables was established based on multi-body system theory and relative pose matrix transformation methods. This model not only achieves precise characterization of system errors for test components on the turntable, but also quantitatively analyzes the influence patterns of fixed and variable errors on system performance.

2. The three-point reverse error separation algorithm effectively compensates for installation eccentricity errors of test components on the turntable. Experimental data demonstrate that this method achieves 96% separation accuracy for spindle roundness errors and 97% for spindle eccentricity errors, fully validating its excellent separation capability for random spindle eccentricity errors.

3. The MPSO+BP neural network model demonstrates significant performance improvements over traditional BP neural networks. Experimental results show that in terms of error compensation effectiveness, this model reduces the system's mean absolute error (MAE) by 75.24% and root mean square error (RMSE) by 71.80%, while improving system accuracy by 73.91%; regarding computational efficiency, when the error converges to 0.1″, the MPSO+BP model requires only 88 iterations to meet the convergence criterion, significantly fewer than the approximately 1000 iterations needed by traditional BP neural networks (a 91.2% reduction), verifying the comprehensive advantages of the MPSO+BP hybrid model in both compensation accuracy and computational efficiency for high-precision angular measurement state compensation.

System calibration and application experiments demonstrate that the system achieves an accuracy of 0.38″. The calibrated system accuracy shows fundamental consistency with factory-calibrated specifications, with post-compensation errors distributed within ±0.5″. These results validate the system's capability for reliable sub-arcsecond high-precision calibration.

Acknowledgments

This research was funded by the Natural Science Foundation of Jilin Provincial of China (NO. 20240101356JC).

References

1. **Huang, M.; Xia, Y. Q.; Li, M. Y.; Tang, Q.** 2019. Calibration of circular division artifacts using a self-developed angle comparator, Optics and Precision Engineering 27(1): 110-120. https://doi.org/10.3788/OPE.20192701.0110.
2. **Ye, C. J.; Zhu, W. B.; Huang, Y.; Zhu, J.; Zhou, W.; Xue, Z.** 2025. A real-time error compensation of rotary table for dynamic angle measurement, Chinese Journal of Sensors and Actuators 38(5): 802-808. https://doi.org/10.3969/j.issn.1004-1699.2025.05.006.
3. **Lou, Z. F.; Liu, L.; Zhang, J. Y.; Fan, K. C.; Wang, X. D.** 2021. A self-calibration method for rotary tables' five degrees-of-freedom error motions, Measurement 174: 109067. https://doi.org/10.1016/j.measurement.2021.109067.
4. **Zhang, R.; Lin, J. R.; Shi, S. D.; Shao, K. P.; Zhu, J. G.** 2023. An angle precision evaluation method of rotary laser scanning measurement systems with a high-Precision turntable, Photonics 10(11): 1224. https://doi.org/10.3390/photonics10111224.
5. **Probst, R.; Wittekopf, R.; Krause, M.; Dangschat, H.; Ernst, A.** 1998. The new PTB angle comparator, Measurement Science and Technology 9(7): 1059-1066. https://doi.org/10.1088/0957-0233/9/7/009.
6. **Estler, W. T.; Queen, Y. H.; Bryan, J.** 1993. An Advanced Angle Metrology System, CIRP Annals 42(1): 573-576. https://doi.org/10.1016/S0007-8506(07)62512-8.
7. **Watanabe, T.; Kon, M.; Nabeshima, N.; Taniguchi, K.** 2014. An angle encoder for super-high resolution and super-high accuracy using SelfA, Measurement Science and Technology 25(6): 065002. https://doi.org/10.1088/0957-0233/25/6/065002.
8. **Guo, Y. T.; Li, X. Y.; Ma, G. F.; Cui, G. T.** 2015. Computation and simulation of global and local spherical harmonic coefficients of asteroid gravity field, Journal of Harbin Institute of Technology 47(5): 13-19. https://doi.org/10.11918/j.issn.0367-6234.2015.05.003.
9. **Xie, J. B.; Zhu, W. B.; Huang, Y.; Zhu, J.; Ma, L.** 2025. Online monitoring method for the accuracy of the rotary table based on its own signals, Chinese Journal of Scientific Instrument 46(11): 106-113. https://doi.org/10.19650/j.cnki.cjsi.J2514522.
10. **Zhang, Y.; Liu, X. M.; Yu, Z,; An, Q.** 2025. Compensation of the industrial robot end effector pose measurement error based on the CSF-PPSO-ESN algorithm, Chinese Journal of Sensors and Actuators 38(9): 1564-1574. https://doi.org/10.3969/j.issn.1004-1699.2025.09.005.
11. **Li, K.; Ding, H. C.; Cao, G. H.; Hou, H.; Zhao, C. F.** 2020. Research on high-precision error measurement system of angular displacements based on reciprocal roll angles, Optical Engineering 59(12): 124110. https://doi.org/10.1117/1.OE.59.12.124110.
12. **Li, K.; Ding, H. C.; Cao, G. H.; Hou, H.** 2022. Error detection system of photoelectric encoder based on optical continuous closed-loop, Infrared and Laser Engineering 51(07): 322-329. https://doi.org/10.3788/IRLA20210715.
13. **Jin, A.; Miao, Y. X.; Liu, D. D.; Lin, J.; Jin, P.; Wang, L.** 2020. Research on spindle dynamic rotation-error-measurement technology, Optics and Precision

Engineering 28(10): 2227-2243. https://doi.org/10.37188/OPE.20202810.2227.
14. **Liu, Y. F.; Ma, X. L.; Ming, P. M.; Chen, J. H.; Liang, X. J.** 2025. Investigation on Energy Output Performance of IPMC Optical-Controlled Composite Driving Based on PLZT Ceramic, Mechanika 31(3): 243-250. https://doi.org/10.5755/j02.mech.40175.
15. **Xie, T.; He, N.; Xie, Q. Y.; Wang, W. B.** 2024. Water-Coal Ratio Control Strategy of Ultra Supercritical Unit Based on Neural Network Inverse Model, Mechanika 30(4): 365-370. https://doi.org/10.5755/j02.mech.35874.

K. Li, W. Wang, K. Wang, X. Yang

RESEARCH ON ERROR CHARACTERISTICS ANALYSIS AND ERROR COMPENSATION METHODS FOR HIGH-PRECISION ANGULAR MEASUREMENT TURNTABLES

S u m m a r y

To address the issues of low calibration accuracy, complex system structure, and cumbersome detection processes in traditional angular measurement equipment, this study proposes an innovative Opto-Mechanical coupled high-precision angular measurement turntable solution based on the principle of reciprocal angular displacement measurement. By systematically analyzing the structural characteristics and error distribution patterns of the turntable, a comprehensive error mathematical model based on relative pose matrices was established, enabling quantitative characterization of the error characteristics in the high-precision angular measurement turntable system. The three-point reverse decoupling algorithm, combined with a systematic continuous error compensation strategy, effectively suppresses installation errors of the components under test on the turntable. Furthermore, by optimizing BP neural network parameters using an improved particle swarm optimization algorithm, the system's error compensation performance was significantly enhanced. Experimental results demonstrate that the compensated system achieves a calibration accuracy of 0.38″, meeting the sub-arc-second precision calibration requirement. The post-compensation overall error distribution remains within ±0.5″, and the reliability and accuracy of the turntable system were thoroughly validated through multiple comparative experiments. This study provides a novel technical approach for high-precision angular measurement.

Keywords: angular measurement, mechanical system, error characteristics, error modeling, error compensation

Received August 15, 2025
Accepted February 20, 2026